Applied Surface Science 752 (2027) 168366

Contents lists available at ScienceDirect

Applied Surface Science

journal homepage: www.elsevier.com/locate/apsusc

Full Length Article

Hematite-modified MWCNT/ionic liquid carbon paste electrodes for selective four-electron oxygen reduction in acidic media

José Ibarra [a], J.R. Sosa-Acosta [a], Rodrigo del Río [a,b], Rodrigo Henriquez [c], Ricardo Faccio [d], Enrique A. Dalchiele [e], Camila Pía Canales [f], Roxana Arce [b,g,*], Galo Ramírez [a,b,**]

[a] Departamento de Química Inorgánica, Facultad de Química, Pontificia Universidad Católica de Chile, Av. Vicuña Mackenna 4860, Casilla 306, Correo 22, Santiago, Chile
[b] Millennium Institute on Green Ammonia as Energy Vector (MIGA), Av. Vicuña Mackenna 4860, Santiago 7820436, Chile
[c] Instituto de Química, Facultad de Ciencias, Pontificia Universidad Católica de Valparaíso, Casilla 4059, Valparaíso, Chile
[d] Área Física & Centro NanoMat, DETEMA, Facultad de Química, Universidad de la República, Av. Gral. Flores 2124, CC 1157, Montevideo CP 11800, Uruguay
[e] Instituto de Física, Facultad de Ingeniería, Universidad de la República, Herrera y Reissig 565, C.C. 30, 11000 Montevideo, Uruguay
[f] Laboratory of Chemical Energy Carriers and Vehicle Systems, Empa Swiss Federal Laboratories for Materials Science and Technology, 8600 Dübendorf, Switzerland
[g] Departamento de Ciencias Químicas, Facultad de Ciencias Exactas, Universidad Andrés Bello, Av. República 275, Santiago 8370146, Chile

ARTICLE INFO

Keywords:
ORR
Acidic media
PGM-free electrocatalyst
Hematite
Carbon paste electrode

ABSTRACT

Developing efficient, stable, and cost-effective electrocatalysts for the oxygen reduction reaction (ORR) in acidic media remains a critical challenge for advancing technologies such as proton exchange membrane fuel cells (PEMFCs). Platinum group metals (PGMs) dominate this field, but they are costly and scarce. This work explores transition metal oxides (TMOs) integrated into a carbon paste matrix as PGM-free alternatives. We synthesized α-Fe_2O_3, Co_3O_4, and $CoFe_2O_4$ nanoparticles and incorporated them into a composite electrode comprising multi-walled carbon nanotubes (MWCNTs) and an N-octylpyridinium hexafluorophosphate ionic liquid (IL) binder. Preliminary electrochemical screening by cyclic voltammetry in O_2-saturated 0.1 M $HClO_4$ suggested a qualitative activity trend: MWCNTs/IL/ α-Fe_2O_3 > MWCNTs/IL/$CoFe_2O_4$ > MWCNTs/IL/Co_3O_4 > MWCNTs/IL. The optimized MWCNTs/IL/α-Fe_2O_3 composite exhibited enhanced ORR performance, with an onset potential of approximately +350 mV vs. RHE and a current density of 11 mA cm^{-2}. Such activity was attributed to a cooperative effect between the well-dispersed α-Fe_2O_3 nanoparticles and the conductive MWCNTs/IL matrix. Electrochemical impedance spectroscopy (EIS) confirmed this interfacial effect, showing that the α-Fe_2O_3 composite had a charge-transfer resistance of 1.05×10^3 Ω, indicating the fastest reaction kinetics among the oxide composites. Furthermore, rotating ring-disk electrode (RRDE) studies demonstrated the catalyst's selectivity, favoring the direct 4-electron pathway to water with minimal hydrogen peroxide production (<10%) across the relevant potential range. The α-Fe_2O_3 system also exhibited operational stability in acidic media, with negligible performance degradation after 100 h under chronoamperometric conditions. These findings highlight the potential of the α-Fe_2O_3-functionalized nanocomposite as a PGM-free cathode material for acidic ORR applications.

1. Introduction

The rising global energy demand and the urgent need to transition toward sustainable systems have positioned fuel cells (FCs) and metal-air batteries (MABs) as key technologies due to their high efficiency and environmental compatibility [1–5]. In these devices, the oxygen reduction reaction (ORR) at the cathode is the rate-limiting process that determines overall performance [6–9]. Currently, platinum (Pt) and its alloys are the benchmark electrocatalysts for the ORR in acidic media; however, their high cost, scarcity, and susceptibility to poisoning significantly hinder large-scale commercial viability [10–13]. Consequently, developing efficient and stable platinum-group-metal-free (PGM-free) electrocatalysts for acidic environments remains a critical challenge [1,14–18]. In this context, achieving a direct 4-electron

* Corresponding author at: Millennium Institute on Green Ammonia as Energy Vector (MIGA), Av. Vicuña Mackenna 4860, Santiago 7820436, Chile.
** Corresponding author at: Departamento de Química Inorgánica, Facultad de Química, Pontificia Universidad Católica de Chile, Av. Vicuña Mackenna 4860, Casilla 306, Correo 22, Santiago, Chile.

https://doi.org/10.1016/j.apsusc.2026.168366
Received 10 June 2026; Received in revised form 28 August 2026; Accepted 8 September 2026
Available online 9 September 2026
0169-4332/© 2026 Elsevier B.V. All rights are reserved, including those for text and data mining, AI training, and similar technologies.

reduction pathway to water is crucial for maximizing energy efficiency and preventing the formation of corrosive peroxide intermediates.

Among the PGM-free alternatives [12,19–27], Fe–N_x-based catalysts have attracted particular attention for acidic ORR owing to their remarkable activity and their ability to approach Pt-like performance under optimized conditions [28,29]. In most of these systems, the active sites are described as atomically dispersed Fe–N_x moieties, often embedded within N-doped carbon matrices, in which the carbon framework plays a dual role: ensuring electrical conductivity and governing site accessibility, porosity, oxygen transport, and the local reaction microenvironment [30]. Recent advances have therefore focused not only on increasing the density of Fe–N_x sites, but also on engineering the surrounding carbon architecture to improve acidic ORR performance [31,32]. Nevertheless, their practical implementation remains limited by durability concerns, including demetallation of Fe centers, carbon corrosion, and degradation of the local coordination environment under acidic operation [23,28–30,33]. These limitations highlight the importance of exploring complementary PGM-free platforms with intrinsically robust, inorganic active phases.

Transition metal oxides (TMOs) such as hematite (α-Fe_2O_3), Co_3O_4, and the mixed spinel $CoFe_2O_4$ have emerged as potential candidates due to their abundance, low cost, and remarkable chemical stability [34–38]. These materials have demonstrated intrinsic electrocatalytic activity, but their implementation in acidic ORR remains challenging due to their low electrical conductivity and limited electrochemically active surface area under low-pH conditions. To overcome such obstacles, it is essential to integrate TMOs into highly conductive frameworks that can facilitate efficient electron transfer and provide a robust environment for the catalytic sites [27,39–43]. Carbon-based nanomaterials, particularly multi-walled carbon nanotubes (MWCNTs), offer a strategic solution by providing a high-surface-area support with excellent electrical conductivity [42–44]. The synergy between TMO nanoparticles and MWCNTs can significantly enhance catalytic performance by preventing nanoparticle aggregation and improving oxygen accessibility to the active sites. Several reports in the literature have supported this strategy [45,46]. For example, Fe_3O_4-decorated CNTs have shown outstanding ORR activity, outperforming 20% Pt/C in alkaline media, attributed to the strong Fe_3O_4/CNT interfacial synergy and improved oxygen accessibility [47]. Likewise, MWCNTs@$ZnMn_2O_4$ composites have been reported to exhibit an onset potential of 0.90 V vs RHE, 99% selectivity toward a four-electron pathway, and high stability, highlighting the beneficial role of strong M−O−C interfacial coupling in promoting efficient ORR kinetics [48].

However, despite the use of MWCNT networks as highly conductive, high-surface-area scaffolds, the catalytic response of these composites in acidic ORR still strongly depends on the interfacial microenvironment surrounding the active sites. In this context, ionic liquids (ILs) have emerged as attractive catalyst-layer modifiers because they can simultaneously act as binders and interfacial promoters, improving catalyst utilization, tuning local hydrophobicity/hydrophilicity, and influencing both oxygen transport and the adsorption of oxygenated intermediates [49–53]. Notably, IL-modified ORR catalyst layers have already shown clear performance gains in benchmark systems: for example, an optimized IL/Pt-C interface has reached a low voltage loss after 30 k accelerated stress cycles, while a later mechanistic study on FeN-type sites showed that IL layers can enhance low-overpotential ORR kinetics by modulating OH binding and, at higher overpotentials, by affecting oxygen solubility/diffusivity within the interfacial layer [54,55]. These advances suggest that ILs should not be regarded merely as inert agglutinants but rather as functional components of the microenvironment that stabilize and activate ORR catalyst interfaces. In line with this rationale, N-octylpyridinium hexafluorophosphate ($OPyPF_6$) has previously demonstrated high mechanical stability and excellent compatibility with MWCNT-based carbon paste matrices in electrochemical systems, thereby enhancing electrocatalytic HER performance [56,57]. In addition, pyridinium-based ionic liquids have been reported to influence the surface chemistry and interfacial properties of transition-metal-based materials, further supporting their role as functional components rather than simple binders [58,59]. These features make $OPyPF_6$ a suitable choice for a MWCNTs/TMO platform, where it is expected to contribute to catalyst-layer integrity and interfacial stabilization under acidic ORR conditions.

The use of carbon paste electrodes (CPEs) modified with all three components (e.g., TMO nanomaterials, MWCNT supports, and ionic liquids) can represent a versatile, cost-effective electrochemical platform. CPEs are characterized by their simple preparation, chemical inertness, and renewable surface, which allow for repeatable measurements by simply extruding and polishing the paste [60,61]. By precisely tuning the ratios of the three components, it is possible to create a highly efficient triple-phase boundary in which gaseous oxygen, the liquid electrolyte, and the solid catalyst coexist. This architectural design will be crucial for optimizing ORR kinetics, ensuring that active centers are fully utilized while maintaining structural stability throughout the reaction in aggressive acidic environments.

In this research, we have engineered a series of composite electrodes based on α-Fe_2O_3, Co_3O_4, and $CoFe_2O_4$, integrated into a MWCNTs/N-octylpyridinium hexafluorophosphate ($OPyPF_6$) IL matrix. We systematically evaluate and compare their ORR electrocatalytic performance in 0.1 M $HClO_4$. Through a comprehensive electrochemical analysis, including rotating ring-disk electrode (RRDE) and electrochemical impedance spectroscopy (EIS), we demonstrate that the α-Fe_2O_3-based composite exhibits superior activity, selectivity for the 4-electron pathway, and enhanced stability. Although $OPyPF_6$ has previously been used as a functional binder/interfacial component in MWCNT-based electrochemical electrodes, and related TMO/MWCNT/IL composites have recently been explored for HER, its full implementation as an integrated platform for acidic ORR remains underexplored. This way, the present study establishes a clear structure-performance relationship, highlighting the potential of such hematite-based nanocomposites as a potential PGM-free catalyst for selective acidic ORR applications.

2. Experimental

2.1. Materials and reagents

All chemicals were of analytical grade and used as received without further purification. Iron(III) chloride hexahydrate ($FeCl_3{\cdot}6H_2O$, 97%), cobalt(II) chloride hexahydrate ($CoCl_2$, 98%), sodium bicarbonate ($NaHCO_3$, ≥99.7%), pyridine (ACS reagent, ≥99.0%), 1-bromooctane (99%), potassium hexafluorophosphate (KPF_6, ≥99%), and silver nitrate ($AgNO_3$, ACS reagent, ≥99.0%) were purchased from Sigma-Aldrich. Ammonium hydroxide solution (NH_4OH, 25%), NaOH, acetonitrile, dichloromethane, ethanol, and perchloric acid ($HClO_4$) were supplied by Merck (Darmstadt, Germany). Ultrapure water with a resistivity of 18.2 MΩ·cm, obtained from a Heal Force Smart-N purification system, was used for the preparation of all aqueous solutions. High-purity oxygen (O_2 99.9%) and argon were supplied by Linde Gas Chile.

2.2. Synthesis and characterization of nanocomposite components

2.2.1. Metal oxide nanoparticles (α-Fe_2O_3, Co_3O_4, $CoFe_2O_4$)

Transition metal oxide nanoparticles were synthesized via controlled co-precipitation using their respective chloride salts as precursors, as described in our previous work [60]. The cobalt oxide (Co_3O_4) synthesis involved a separate aqueous solution of $CoCl_2$ and $NaHCO_3$ at a 1:1 M ratio. The cobalt precursor was stirred for 15 min, followed by the dropwise addition of the bicarbonate solution under constant agitation. To regulate precipitation, the reaction was maintained in an ice bath. After 15 min, the precipitate was isolated by centrifugation, washed with distilled water, and dried at 100 °C. The final crystalline structure was obtained by calcination at 600 °C for 2 h in a tube furnace. Hematite nanoparticles (α-Fe_2O_3) were produced by dissolving 10 g of $FeCl_3$ $6H_2O$

in 50 mL of distilled water at room temperature. Under continuous stirring, a 25% m/m NH_4OH solution was introduced at a controlled rate of 1 mL/min. The mixture was stirred for 1 h, maintaining a constant pH of 12 throughout. The resulting suspension was evaporated at 100 °C for 2 h, and the recovered brown powder was subsequently annealed at 500 °C for 4 h in air to achieve the desired phase. The cobalt ferrite ($CoFe_2O_4$) mixed spinel structure was synthesized by mixing 0.4 M $FeCl_3$ and 0.2 M $CoCl_2$ solutions in ultrapure water to ensure the appropriate stoichiometry. Precipitation was triggered by the slow, dropwise addition of 3 M NaOH until the pH reached 11–12. The slurry was then aged at 80 °C for 1 h with constant stirring, then cooled to room temperature. The product was purified through multiple washing cycles with ultrapure water and ethanol, followed by centrifugation at 3000 rpm for 15 min. The isolated black precipitate was dried at 100 °C for 12 h and ground into a fine powder. Finally, the material was calcined at 600 °C for 10 h to eliminate residual water and ensure complete crystallization.

2.2.2. N-octylpyridinium hexafluorophosphate ionic liquid

The N-octylpyridinium hexafluorophosphate ionic liquid was synthesized through a two-stage procedure, as established in our previous work [60]. Initially, the N-octylpyridinium bromide precursor was prepared by combining pyridine (10 mL), 1-bromooctane (21.5 mL), and acetonitrile (20 mL) in a synthesis flask. The mixture was refluxed at 100 °C under a constant argon atmosphere and with continuous stirring for 48 h. Following the reaction, the solvent was removed via evaporation, and the intermediate product was dried at 70 °C for 15 h. In the second stage, 12.54 g of N-octylpyridinium bromide and 8.70 g of potassium hexafluorophosphate (KPF_6) reacted in a biphasic system consisting of 20 mL of water and 20 mL of dichloromethane. This mixture was stirred at room temperature for 2 h to facilitate the anion exchange. The resulting solution was transferred to a separating funnel, where the organic phase was isolated and washed repeatedly with ultrapure water. The complete removal of residual bromide ions was confirmed by testing the aqueous washings with $AgNO_3$ until no precipitate was detected. Finally, the organic solvent was removed, yielding a white, serous solid, which was further purified by recrystallization from 95% ethanol.

2.2.3. Physicochemical characterization

Surface elemental composition and chemical oxidation states were analyzed by X-ray Photoelectron Spectroscopy (XPS) using a FlexPS system from SPECS. This system comprises a hemispherical analyzer model PHOBIOS 150 and a 1D-DLD detector, with a monochromatic X-ray source model FOCUS 500 emitting Al Kα radiation at 1486.71 eV. Binding energies were charge-corrected by referencing the graphitic C 1s (sp^2, C=C) peak of the MWCNTs to 284.5 eV for all composite samples. For the α-Fe_2O_3 NPs, the spectra were referenced to the adventitious C 1s peak at 284.8 eV. Additionally, the N-octylpyridinium hexafluorophosphate ionic liquid was characterized by ^1H NMR. The systematic physicochemical characterization of the IL together with detailed FE-SEM characterization of the transition-metal oxide nanoparticles is reported in our previous work [60].

2.3. Electrode preparation

Working electrodes were fabricated using a modified carbon-paste method to ensure high conductivity and mechanical stability. The composite paste was prepared by accurately weighing and mixing 0.035 g of MWCNTs with 0.035 g of the corresponding transition-metal oxide. For the modified electrodes, 0.02 g of the synthesized ionic liquid was incorporated as a binder, and 72 μL of mineral oil was added as an auxiliary binder. Meanwhile, for the control sample prepared in the absence of the ionic liquid, 0.07 g of MWCNTs was used, and mineral oil was used as the primary binding agent, with the mixture brought to 0.09 g of MWCNTs carbon paste. The homogenization process was performed in an agate mortar, where the components were physically ground together. Small aliquots of diethyl ether were added during mixing to facilitate the dispersion of the nanomaterials within the binder matrix. The grinding continued until the solvent had completely evaporated at room temperature. 15 mg of the resulting mixture was packed into a hollow Teflon rod (geometric area = 0.03 cm^2) to form a conductive column. The electrode was then heated at 70 °C for 1 h to promote a uniform distribution of the ionic-liquid binder, eliminate the volatile solvent, and establish a robust boundary among the solid catalyst, the conductive support, and the electrolyte. This fabrication method ensures that the surface-active sites are effectively utilized during ORR.

2.4. Electrochemical measurements

All electrochemical measurements were performed at room temperature (~25 °C) using a CH-Instrument CHI750D (CH Instruments, Austin, TX, USA) potentiostat in a conventional three-electrode cell. The prepared carbon paste electrode served as the working electrode, Ag/AgCl (3 M KCl) as the reference, and a platinum wire as the counter electrode. The electrolyte for all experiments was an O_2- or Ar-saturated 0.1 M $HClO_4$ aqueous solution (pH = 1). All potentials were reported against the Reversible Hydrogen Electrode (RHE) scale, calculated using the following equation:

$$E_{RHE} = E_{Ag/AgCl} + 0.0591\ pH + 0.1976\ V \quad (1)$$

To evaluate the electrocatalytic activity, a systematic selection procedure was adopted, consisting of an initial qualitative screening followed by a quantitative validation of the more active composite. Before each experiment, the working electrode was conditioned by 10 potential cycles to ensure a stable surface. Cyclic Voltammetry (CV) screenings were performed at a scan rate of 50 mV/s. Electrochemical Impedance Spectroscopy (EIS) was carried out at −250 mV vs RHE over a frequency range of 100 kHz to 1 Hz with a 5 mV AC amplitude. Data was analyzed using ZView software. The electrochemical stability of the optimal system was evaluated using complementary short- and long-term stability protocols under ORR conditions in O_2-saturated 0.1 M $HClO_4$. First, cyclic voltammetry (CV) was recorded before and after 50 consecutive potential cycles to assess changes in the electrochemical response upon repeated polarization. Long-term operational stability was subsequently evaluated by chronoamperometry for 100 h at −0.25 V vs. RHE under continuous O_2 bubbling. After 2 h of electrolysis, the electrolyte was collected for Fe-leaching analysis, while the recovered composite was used for microscopic characterization. Potential Fe dissolution was quantified by inductively coupled plasma optical emission spectrometry (ICP-OES) using an Agilent 5800 ICP-OES spectrometer (Agilent Technologies). A 5.0 mL aliquot of the electrolyte was diluted to 10.0 mL prior to analysis, and Fe was monitored using the 238.204 nm emission line against external certified Fe calibration standards; the reported concentrations were corrected for the corresponding dilution factor. The morphology, nanostructure, and local integrity of the optimal composite before and after the cathodic regime were examined by high-resolution transmission electron microscopy (HRTEM) using a FEI Talos F200X microscope operated at 200 kV. These complementary electrochemical, elemental, and microscopic measurements were employed to evaluate the operational stability of the composite and to characterize possible modifications induced by prolonged cathodic polarization under acidic ORR conditions.

Hydrodynamic Measurements (RDE/RRDE) were conducted using an RRDE-3A (ALS Co., Ltd, Japan) setup with a paste compartment (5.0 mm diameter) and a Pt ring, for Levich analysis, polarization curves were recorded at a scan rate of 50 mV/s while varying the rotation speed from 400 to 1600 rpm. The plot of limit current vs. $\omega^{1/2}$ was interpreted with the Levich equation:

$$IL = 0.62 \cdot n \cdot F \cdot A \cdot D_O^{2/3} \cdot \omega^{1/2} \cdot v^{-1/6} \cdot C_O \quad (2)$$

For ORR selectivity analysis, the electrode rotated at a constant 1600 rpm with a scan rate of 5 mV/s, while the ring potential was held at 1.2 V vs. RHE for H_2O_2 detection. To calculate n and $\%H_2O_2$, the following

equations were used:

$$n = 4x\frac{id}{id + \frac{ia}{ec}} \quad (3)$$

$$\%H_2O_2 = 2x\frac{\frac{ia}{ec}}{id + \frac{ia}{ec}} \quad (4)$$

where *id*, *ia*, and *ec* represent the disk current, ring current, and collection efficiency (ec = 0.43), respectively.

3. Results and discussion

3.1. Electrochemical studies

To preliminarily examine the electrocatalytic response of the non-precious-metal oxide composites toward ORR in acidic media, a series of catalysts was prepared and first analyzed by cyclic voltammetry (Fig. 1a). This initial screening allowed a qualitative comparison of the cathodic response in O_2-saturated 0.1 M $HClO_4$. A clear preliminary trend in activity performance was established among the materials: MWCNTs/IL/α-Fe_2O_3 > MWCNTs/IL/$CoFe_2O_4$ > MWCNTs/IL/Co_3O_4 > MWCNTs/IL. The MWCNTs/IL/α-Fe_2O_3 composite electrode shows an ORR onset potential of +350 mV vs. RHE and a peak current density of −11 mA·cm^{-2}. The enhanced performance of the iron oxide system suggests that iron's intrinsic properties are fundamental to the catalytic process. We attribute this to the electrophilic nature of Fe(III) sites and the potential presence of a dynamic mixed-valence Fe(III)/Fe(II) interface, which favors the adsorption and subsequent activation of O_2 molecules [62–64]. While $CoFe_2O_4$ shows moderate activity, likely due to a Co-Fe presence [65], the performance of Co_3O_4 is slightly better than the bare carbon support, underscoring the critical role of iron in this catalytic system. To examine the origin of the α-Fe_2O_3 composite's activity, a control study was performed (Fig. 1b). The electrode containing only α-Fe_2O_3 and the ionic liquid (IL/α-Fe_2O_3) exhibits negligible faradaic current, confirming the poor intrinsic conductivity of the bare oxide. The MWCNTs/IL support shows lower ORR activity than the final MWCNTs/IL/α-Fe_2O_3 composite, indicating that the activity is not merely additive but a demonstrably cooperative effect, far exceeding the simple sum of its components. This interfacial effect arises from the MWCNTs/IL network, which provides a high surface area and an electrically conductive scaffold. This architecture ensures both efficient charge transport to the α-Fe_2O_3 nanoparticles and maximal exposure of their catalytically active sites to the electrolyte, thus validating the rational design of our composite electrode [60,65].

To further investigate the kinetics of the oxygen reduction reaction (ORR) at the electrode electrolyte interface, and to validate the trend obtained by cyclic voltammetry, electrochemical impedance spectroscopy (EIS) was performed. The resulting Nyquist plots (Fig. 2a) are dominated by semicircles at high to medium frequencies, characteristic of charge-transfer-limited processes. The diameters of these semicircles correspond to the charge-transfer resistance (Rct), a key indicator of catalytic activity [66,67]. Quantitative analysis was performed by fitting the experimental data to appropriate equivalent circuit models. A simple Randles circuit adequately modeled the impedance response of the bare MWCNTs/IL paste and the $CoFe_2O_4$ composite, while a Randles circuit modified with an open Warburg element, accounting for diffusion limitations, provided a better fit for the α-Fe_2O_3 and Co_3O_4 systems. Crucially, the MWCNTs/α-Fe_2O_3 composite prepared without the ionic liquid exhibited two distinct relaxation processes in the Bode plot, which could be attributed to the ORR and potential acid-induced leaching of the iron oxide. To account for this second process, the equivalent circuit was modified by adding an additional resistance and another constant phase element (CPE). The fitting for this nanocomposite yielded an Rct of 2.86 × 10^4 Ω, suggesting that the ionic liquid may contribute to modifying the interfacial environment around the oxide particles and potentially favor their stabilization in the acidic medium. The fitted parameter (Table 1) reveals a Rct of 2.31 × 10^4 Ω for the bare MWCNTs/IL paste, confirming its lower intrinsic activity.

In contrast, the incorporation of metal oxide nanoparticles clearly lowers the Rct of the composites. The α-Fe_2O_3 composite exhibits a Rct of 1.05 × 10^3 Ω, followed by $CoFe_2O_4$ (1.14 × 10^3 Ω) and then Co_3O_4 (2.65 × 10^3 Ω). This quantitative trend directly corroborates the enhanced activity observed for the α-Fe_2O_3 electrode in the voltammetric measurements (Fig. 1). The frequency-dependent behavior, detailed in the Bode plots (Fig. 2b and c), provides complementary insights. The impedance magnitude (|Z|) at low frequencies (Fig. 2b) shows a similar behavior, with the α-Fe_2O_3 composite showing the lowest overall impedance. More revealingly, the phase angle plot (Fig. 2b) highlights differences in the characteristic time constants of the charge transfer processes. The primary phase angle maximum for the

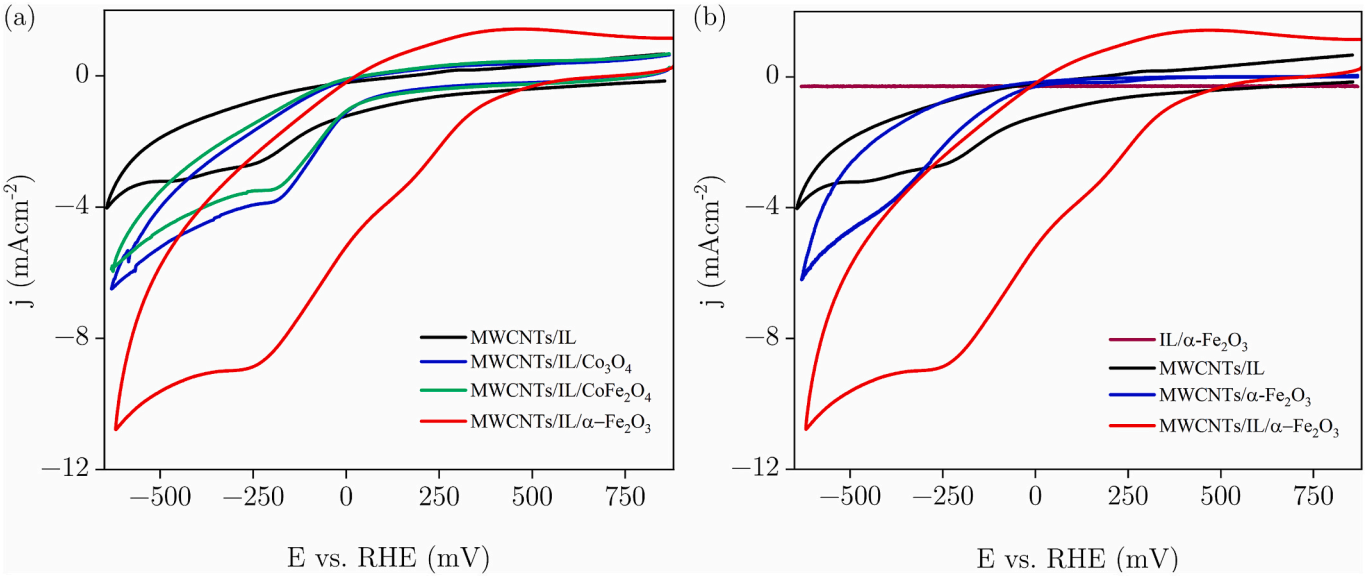


Fig. 1. Cyclic voltammograms of the different prepared electrodes in O_2-saturated 0.1 M $HClO_4$ solution at a scan rate of 50 mV/s. **(a)** Comparison of the ORR activity for the bare MWCNTs/IL paste and composites containing Co_3O_4, $CoFe_2O_4$, and α-Fe_2O_3. **(b)** Comparative analysis of the full MWCNTs/IL/ α-Fe_2O_3 composite with its individual components.

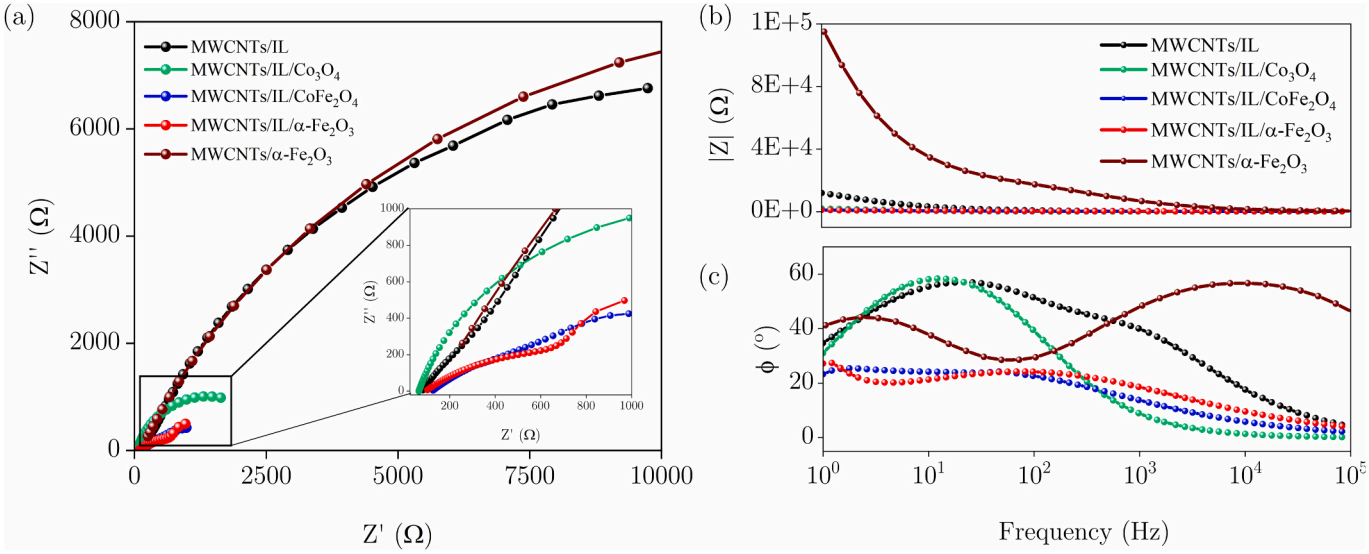


Fig. 2. EIS analysis of the different catalyst systems, recorded at −250 mV vs RHE in O_2-saturated 0.1 M $HClO_4$. **(a)** Nyquist plots, with an inset showing a magnified view of the high-frequency region. Corresponding Bode plots showing impedance magnitude |Z| **(b)** and phase angle (Φ) as a function of frequency **(c)**.

Table 1
Solution resistance (Rs), charge transference resistance (Rct), and constant phase element (CPE) values for the studied nanocomposites.

Nanocomposite electrocatalyst	Rs (Ω)	Rct (Ω)	CPE-P
MWCNTs/α-Fe_2O_3	124,6	2.86×10^4	0.74
MWCNTs/IL	84,5	2.31×10^4	0.69
MWCNTs/IL/ Co_3O_4	64.8	1.65×10^3	0.82
MWCNTs/IL/α-Fe_2O_3	94,2	1.05×10^3	0.80
MWCNTs/IL/ $CoFe_2O_4$	121.9	1.14×10^3	0.52

α-Fe_2O_3 system occurs at a higher frequency (indicating a faster process) than for the $CoFe_2O_4$ and Co_3O_4 systems, while the bare paste exhibits its main capacitive/resistive response at significantly lower frequencies. This shift towards higher frequencies in α-Fe_2O_3 reinforces its faster charge-transfer kinetics. However, such behavior could also be influenced by variations in the capacitive response or the specific surface properties of the different transition metal oxides, so this frequency shift should be interpreted as an overall indicator of improved interfacial charge-transfer efficiency. In conclusion, both Nyquist and Bode analyses consistently demonstrate the superior kinetic performance of the α-Fe_2O_3 catalyst for the ORR in acidic media, confirming its suitability for further detailed investigation.

3.2. *Long-term stability and post-ORR surface evolution*

Having identified the MWCNTs/IL/α-Fe_2O_3 composite as the more active material, the investigation proceeded to assess its suitability for ORR by probing its catalytic selectivity and long-term durability. First, a control experiment was conducted in an Ar-purged electrolyte to distinguish the ORR signal from any intrinsic redox activity of the material itself (Fig. 3a). The resulting voltammogram shows no significant faradaic features within the relevant potential window. This provides direct evidence that the large cathodic current observed in the O_2-saturated solution is exclusively attributable to ORR electrocatalysis. Notably, the onset of the hydrogen evolution reaction (HER) becomes apparent at highly negative potentials (−500 mV vs. RHE), a reaction that is effectively masked by the mass-transport-limited ORR current in the main experiment. Next, the catalyst's operational stability was assessed using a preliminary stability test comprising 50 consecutive potential cycles. As depicted in Fig. 3b, the polarization curve recorded after the test shows activity nearly identical to that of the initial voltammogram. The catalyst exhibits only a negligible loss in current density and no discernible negative shift in its half-wave potential, confirming its durability.

Long-term operational stability was further evaluated by chronoamperometry for 100 h at −0.25 V vs. RHE in O_2-saturated 0.1 M $HClO_4$ (Fig. 3c). The MWCNTs/IL/α-Fe_2O_3 electrode showed an initial increase in the magnitude of the cathodic current, from approximately −4.3 to −6.0 mA/cm^2 during the first ~30 h, followed by a prolonged quasi-steady-state response of approximately −6.0 to −7.0 mA/cm^2 up to 100 h. The initial period could be assigned to an electrochemical conditioning regime, a behavior particularly relevant for the present porous carbon-paste architecture, in which progressive electrolyte penetration and wetting of the MWCNTs/IL/α-Fe_2O_3 network can gradually increase the fraction of electrochemically accessible material, facilitate ionic transport through the confined porous structure, and expose additional oxide/carbon interfacial sites [68,69].

In parallel, the strongly cathodic polarization conditions may promote changes in the surface redox state of the iron oxide, including partial reduction of Fe(III) and the possible development of mixed-valence Fe environments. Accordingly, the measured cathodic current should not be interpreted as arising exclusively from ORR, since parallel processes such as proton reduction and cathodically induced modification of the oxide surface may also contribute under these conditions. Nevertheless, after the initial conditioning period, the absence of a sustained decrease in current over the subsequent tens of hours indicates that the composite maintains a stable electrochemically active interface during prolonged acidic operation.

To directly evaluate whether this cathodic operation was accompanied by dissolution of the iron oxide component, the electrolyte collected after 2 h of electrolysis was analyzed by ICP-OES. The Fe emission response at 238.204 nm for the post-electrolysis electrolyte was essentially comparable to that of the 0.1 M $HClO_4$ blank, with both remaining below the method's analytical reporting limit (<0.1 ppm); the corresponding ICP-OES emission spectra are provided in the Supporting Information (**Fig. S1**). Considering the total electrolyte volume of 15 mL, this concentration corresponds to an upper limit of <1.5 μg of Fe in the complete electrolyte, equivalent to less than approximately 0.04–0.06% of the estimated Fe initially contained in the electrode. Therefore, no quantifiable increase in dissolved Fe was detected after electrolysis relative to the acidic electrolyte blank. Although Fe release below the analytical reporting limit cannot be excluded, these results demonstrate that substantial Fe leaching does not occur during the

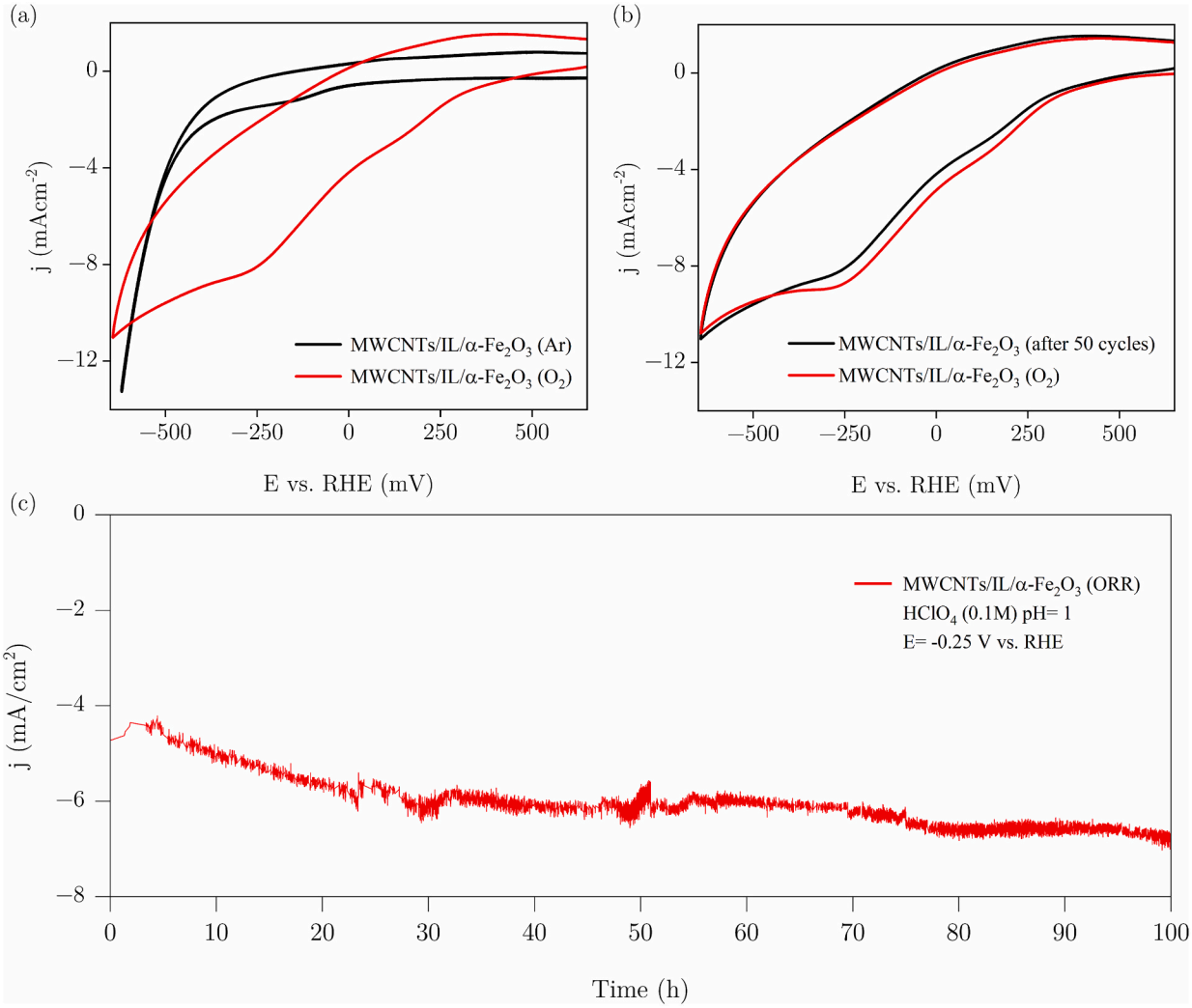


Fig. 3. Electrochemical characterization of MWCNTs/IL/α-Fe_2O_3 catalyst. **(a)** Control experiment showing the cyclic voltammogram in O_2-saturated vs. Ar purged 0.1 M $HClO_4$ solution. **(b)** Short-term stability test comparing the initial CV (cycle 1) with the CV recorded after 50 continuous cycles in O_2-saturated electrolyte. Scan rate: 50 mV/s. And **(c)** Long-term chronoamperometry of the MWCNTs/IL/α-Fe_2O_3 catalyst in a constant O_2 purged 0.1 M $HClO_4$ solution at −250 mV vs. RHE.

investigated electrochemical treatment and indicate that reductive dissolution of α-Fe_2O_3 is not a dominant degradation pathway under these conditions.

Consistent with the ICP-OES results, post-ORR electron microscopy provided additional evidence of the morphological integrity of the MWCNTs/IL/α-Fe_2O_3 composite after prolonged electrochemical operation. Representative HRTEM images acquired before and after the 100 h ORR stability test are shown in Fig. 4**(a–d)**. Prior to ORR, α-Fe_2O_3 nanoparticles are observed as nanosized aggregates distributed over and in close contact with the MWCNT network, while the nanotubes retain their characteristic elongated tubular morphology Fig. 4**(a,b)**. Particle-size analysis yielded an average particle size of 12.80 ± 2.36 nm. After 100 h of operation (Fig. 4**(c,d)**), the composite preserves the same overall morphology, with α-Fe_2O_3 nanoparticles remaining associated with the MWCNT framework and no evident collapse or fragmentation of the carbon nanotube network. Importantly, the average nanoparticle size remained essentially unchanged at 12.85 ± 1.38 nm. The absence of a measurable increase in particle size indicates that prolonged cathodic polarization does not promote significant nanoparticle coalescence or electrochemically induced sintering. Likewise, no obvious morphological evidence of extensive oxide dissolution is observed.

3.3. XPS analysis for the composite paste

X-ray photoelectron spectroscopy (XPS) was employed to probe the surface chemical states and interfacial evolution of the Fe_2O_3-based composite before and after ORR (Fig. 5). As shown in Fig. 5a, the Fe 2p spectrum of the synthesized hematite NPs exhibits the characteristic multiplet-split of Fe $2p_{3/2}$–$2p_{1/2}$ envelope of high-spin Fe(III), together with the corresponding shake-up/charge-transfer satellite around 717.4 eV, consistent with pristine hematite [70–72]. In the composite before ORR (Fig. 5b), the Fe 2p region retains a predominantly Fe(III)-like lineshape. After ORR, the Fe 2p spectrum shows attenuation of the Fe (III) satellite response together with the appearance of an additional contribution in the Fe $2p_{3/2}$ region at 707.35 eV. Such a low binding energy signal is considerably lower than that typically associated with Fe(II) oxides, whose Fe $2p_{3/2}$ intensity is generally located around 709–710 eV, and is instead close to the characteristic position of metallic Fe^0 at approximately 706.6–707.0 eV [73]. Accordingly, this contribution is tentatively assigned to metallic or highly reduced Fe^0-like surface species. This assignment is electrochemically plausible because the ORR cycling window was extended to approximately −0.65 V vs RHE in pH 1 $HClO_4$, corresponding to strongly reducing conditions near the Fe^{2+}/Fe^0 equilibrium potential according to Pourbaix diagrams [74]. Under such cathodic polarization, reduction of hematite may proceed through

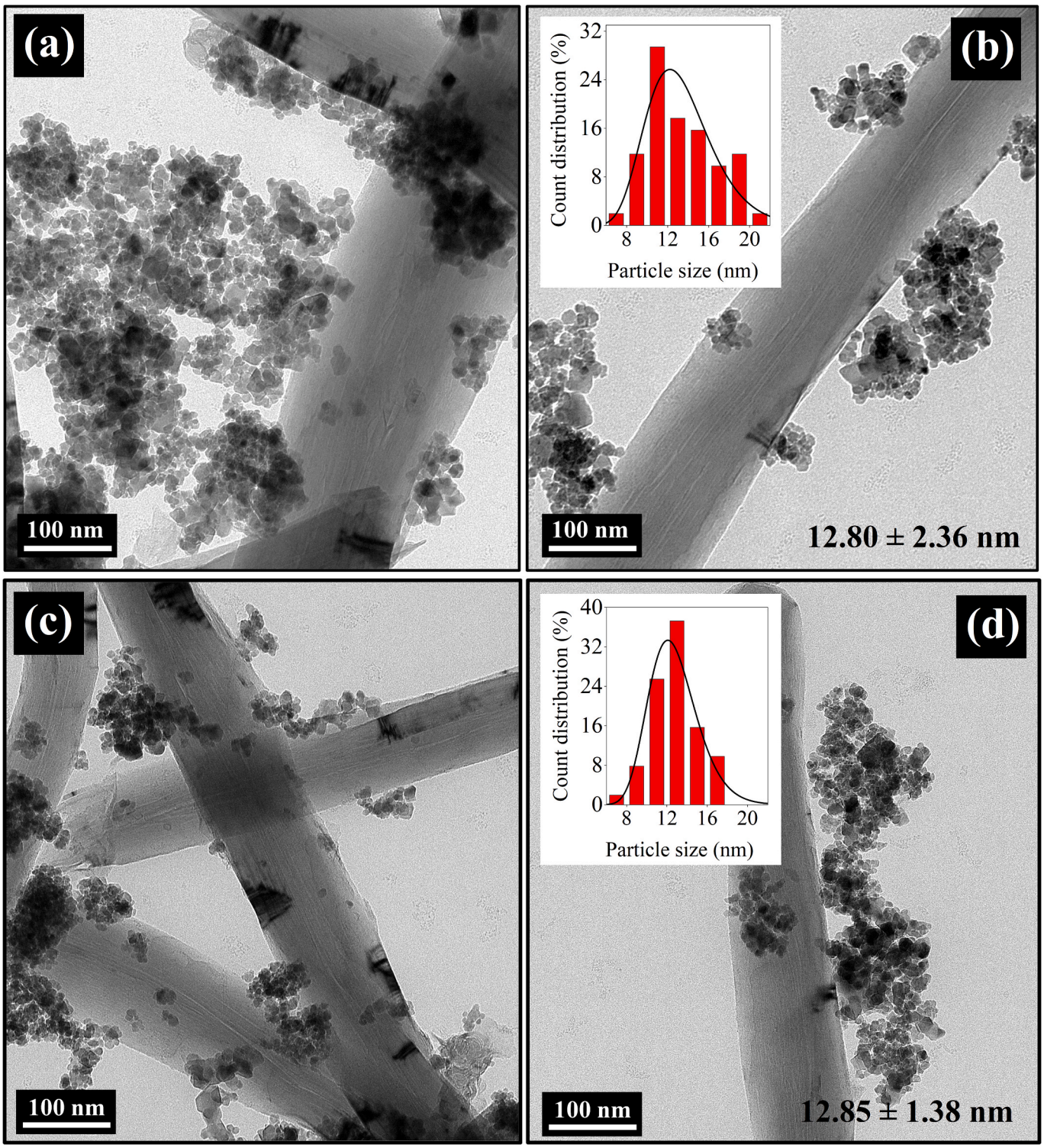


Fig. 4. Representative HRTEM images of the MWCNTs/IL/α-Fe_2O_3 composite **(a,b)** before and **(c,d)** after the 100 h ORR stability test in O_2-saturated 0.1 M $HClO_4$. The inset represents the corresponding nanoparticle size distributions.

successive Fe(III) → Fe(II) conversion, potentially involving transient mixed-valence Fe_3O_4-like or reduced FeO_x interfacial domains, followed by partial formation of Fe^0 [73,75]. Therefore, the post-ORR surface is more appropriately described as a chemically heterogeneous Fe(III)/Fe(II)/Fe^0 interphase rather than as the product of a simple Fe(III)-to-Fe(II) conversion. Nevertheless, because of the strongly overlapping multiplet and satellite structure of the Fe 2p region, the Fe_3O_4-like and Fe^0 assignments should be regarded as evidence of partial surface reduction rather than quantitative identification of discrete bulk phases.

This interpretation was supported by the O 1s analysis (Fig. 5c). For the composite before ORR, the O 1s envelope is dominated by contributions in the 531–533 eV range, with a major C–O component at 531.5 eV (45.0%), a smaller O–H/Fe–OH contribution at 530.8 eV (7.3%), and adsorbed H_2O at 532.8 eV (20.2%), indicating that the near-surface oxygen signal is strongly influenced by oxygenated carbon/ionic-liquid functionalities rather than by the oxide lattice oxygen alone

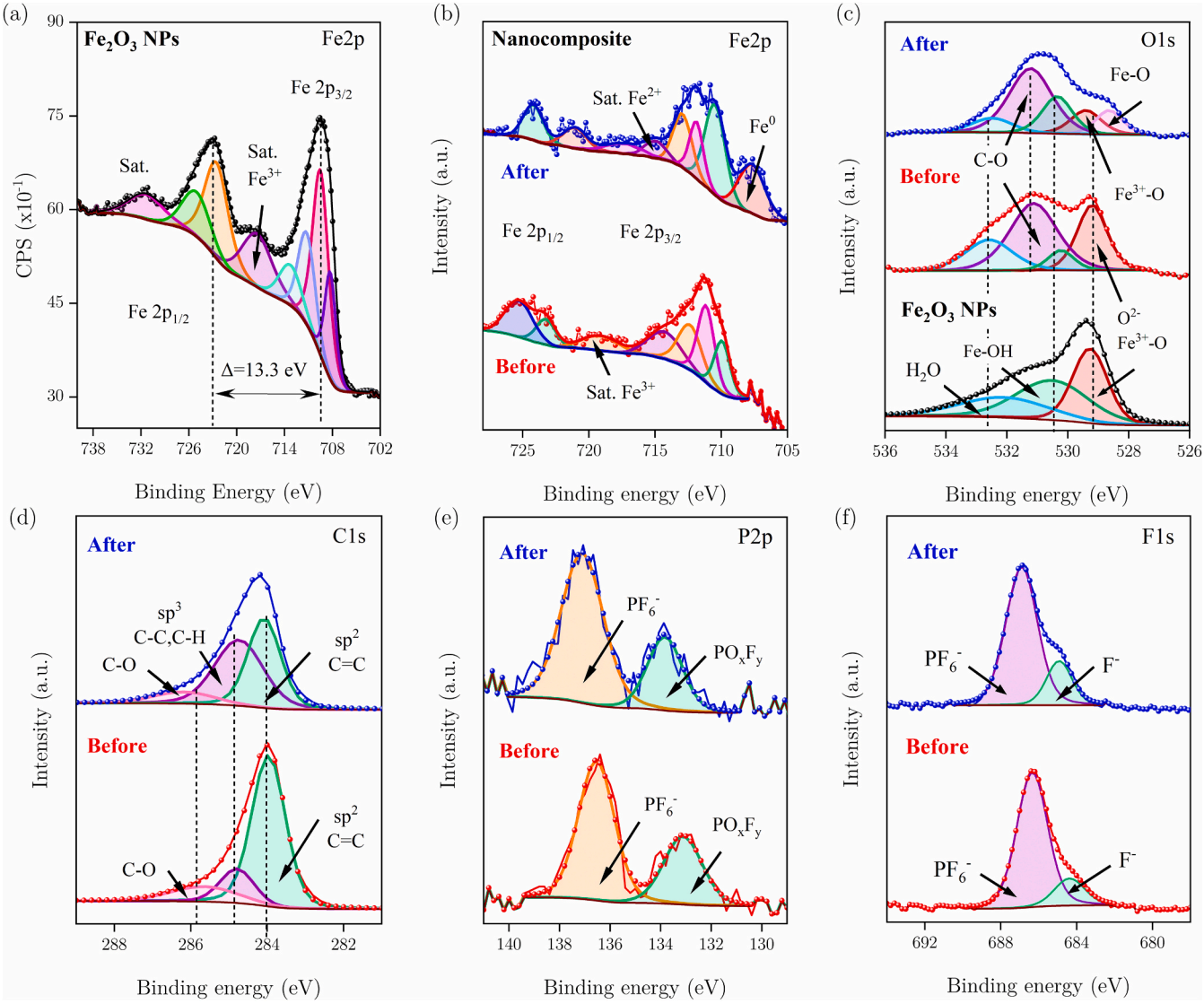


Fig. 5. XPS spectra of synthesized α-Fe_2O_3 nanoparticles incorporated in the MWCNTs/ionic-liquid (N-octylpyridinium PF_6) composite before and after ORR. **(a)** Fe 2p spectrum of pristine Fe_2O_3 NPs **(b)** Comparative Fe 2p spectra of the composite before (red) and after ORR (blue). **(c)** O 1 s spectra for Fe_2O_3 NPs (black) and the composite before/after ORR **(d)** C 1 s spectra for the composite before/after ORR **(e)** P 2p spectra **(f)** F 1 s spectra. Solid lines correspond to the fitted envelopes, and colored components represent individual peak contributions.

(529.5 eV, 27.4%). Supporting information includes Table S1, which provides quantitative parameters for the XPS fitting analysis. In contrast, after ORR, the O 1 s region required an additional low-binding-energy lattice component at 529.2 eV assigned to a reduced Fe–O environment, contributing 14.6% of the fitted area, together with a remanent Fe^{3+} lattice contribution at 529.9 eV (25.0%). At the same time, the O–H/Fe–OH component increases markedly from 7.3% to 18.4%, whereas the adsorbed H_2O contribution decreases from 20.2% to 6.2%. These changes indicate that ORR drives the formation of a mixed-valent, more hydroxylated near-surface FeOx layer rather than the simple accumulation of weakly bound oxygenated adsorbates. From a functional standpoint, the emergence of mixed Fe^{2+}/Fe^{3+} near-surface environments is expected to modify the local Fe 3d occupancy, thereby facilitating O_2 adsorption/activation and interfacial electron transfer [64]. Concurrently, the stronger Fe–OH/O–H contribution suggests a surface better adapted to proton-coupled oxygen reduction steps. Thus, these XPS results support the notion that the active surface after ORR is electronically and chemically distinct from the as-prepared state, with a more heterogeneous and catalytically responsive FeOx interphase.

Fig. 5d–f tracks the evolution of the c 1s, P 2p, and F 1s regions of the composite before and after ORR. In the C 1s high-resolution spectra, the carbon envelope before ORR is dominated by the graphitic C=C (sp2) contribution at 283.96 eV (70.2%), together with smaller C–C/C–H (sp3-like) and C–O components. After ORR, the sp3-like contribution increases substantially from 16.0% to 46.6%, becoming comparable to or slightly greater than the sp2 component (43.0%), while C–O remains clearly detectable. Importantly, this increase in the sp3-like contribution may indicate interfacial restructuring of the carbon/ionic-liquid phase during operation, likely increasing the relative near-surface contribution of aliphatic IL-derived carbon and/or defect-associated carbon at the MWCNTs/oxide interface without evidence of severe degradation of the carbon framework.

The anion-related signatures of the ionic liquid are reflected in the P 2p and F 1s regions. In both states, the dominant contribution remains PF_6^-, confirming that the ionic liquid is still a major surface constituent after ORR. At the same time, the P 2p spectra show a lower-binding-energy component assigned to POxFy, both before and after ORR, evidencing partial PF_6^- transformation during film preparation and/or ambient handling, and its persistence under electrochemical conditions. Consistently, the F 1s spectra displayed a lower-binding-energy

contribution assigned to inorganic fluoride or metal-fluoride-like environments (F^-/M−F), which increases from 16.5% before ORR to 20.5% after ORR. In the present system, this component is most reasonably associated with Fe–F-type interfacial environments generated from partial PF_6^- hydrolysis/defluorination. Importantly, because PF_6^- remains dominant whereas F^-/M−F and POxFy remain secondary but persistent, the XPS data do not suggest severe ionic-liquid degradation. Rather, they support the formation of a thin fluorinated/oxyfluorophosphate-containing interphase that may contribute to surface stabilization by passivating the catalyst/electrolyte interface while maintaining the ionic-liquid-rich environment. Taken together with the Fe 2p and O 1 s results, these observations support a scenario in which ORR promotes both redox/hydroxylation of near-surface Fe–O environments and controlled chemical evolution of the carbon/ionic-liquid interphase, providing a chemically plausible basis for the improved catalytic response and interfacial stability.

3.4. Rotating ring-disk and kinetics studies

To elucidate the reaction pathway selectivity and quantify hydrogen peroxide (H_2O_2) production of the more active system (MWCNTs/IL/α-Fe_2O_3), rotating ring-disk electrode (RRDE) voltammetry was performed. To highlight the impact of the iron oxide on reaction selectivity, the performance of the α-Fe_2O_3 composite was directly compared to that of the bare MWCNTs/IL support using RRDE voltammetry. A comparison of the voltammograms (Fig. 6, top panels) reveals that while the bare support (Fig. 6a) generates a substantial ring current indicative of significant H_2O_2 formation, the ring current for the α-Fe_2O_3 composite (Fig. 6b) is suppressed to a nearly negligible level. This observation is quantified in the lower panels. For the α-Fe_2O_3 catalyst (Fig. 6d), the calculated number of transferred electrons (n) remains stable at ~3.8–4.0 across the entire potential window of interest, with a corresponding H_2O_2 yield consistently around 5–7%.

On the other hand, the bare support **(c)** exhibits an inefficient pathway, with n starting as low as 2.4 and a peroxide yield reaching up to 80%. This confirms that the α-Fe_2O_3 nanoparticles are not only active but also selective to the 4-electron ORR pathway. This selectivity, combined with the previously demonstrated activity and stability, solidifies the MWCNTs/IL/α-Fe_2O_3 composite as an effective catalyst for the complete reduction of oxygen to water.

The ORR kinetics on the α-Fe_2O_3 catalyst were further studied using rotating disk electrode (RDE) voltammetry (Fig. 7a). The hydrodynamic voltammograms exhibit well-defined, mass-transport-limited current plateaus that increase systematically with the rotation rate (ω). Quantitative analysis of the polarization curve at 1600 rpm reveals an onset potential (E_{onset}) of 0.41 V vs. RHE and a half-wave potential ($E_{1/2}$) of

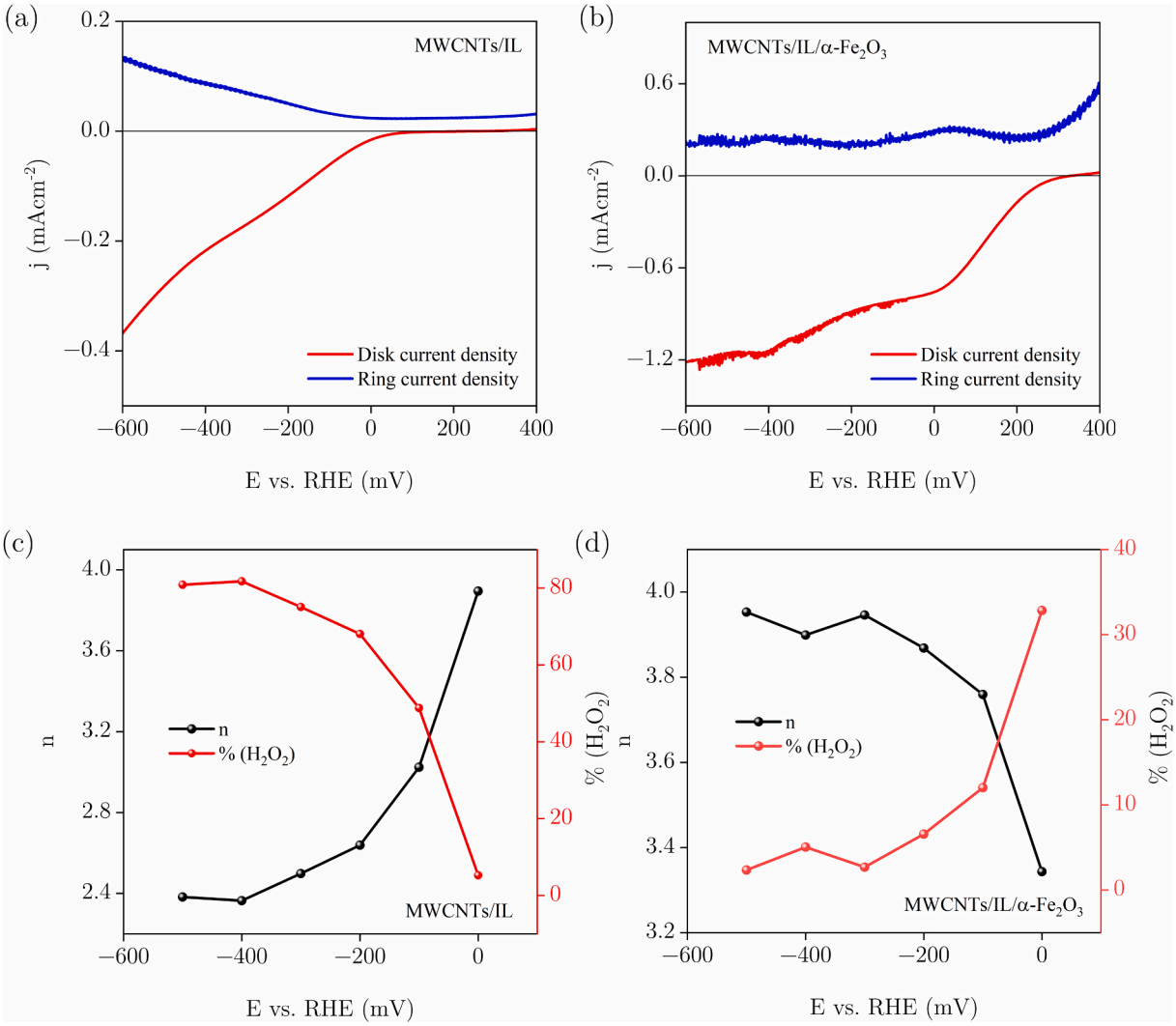


Fig. 6. RRDE analysis for the ORR. Top panels: Disk (solid red line) and ring (blue line) currents for **(a)** the bare MWCNTs/IL support and **(b)** the MWCNTs/IL/α-Fe_2O_3 catalyst. Bottom panels: Calculated number of transferred electrons (n) and H_2O_2 yield for **(c)** the bare support and **(d)** the α-Fe_2O_3 catalyst. Conditions: 1600 rpm, O_2-saturated 0.1 M $HClO_4$, scan rate 5 mV/s. The ring potential was held at 1.2 V vs. RHE.

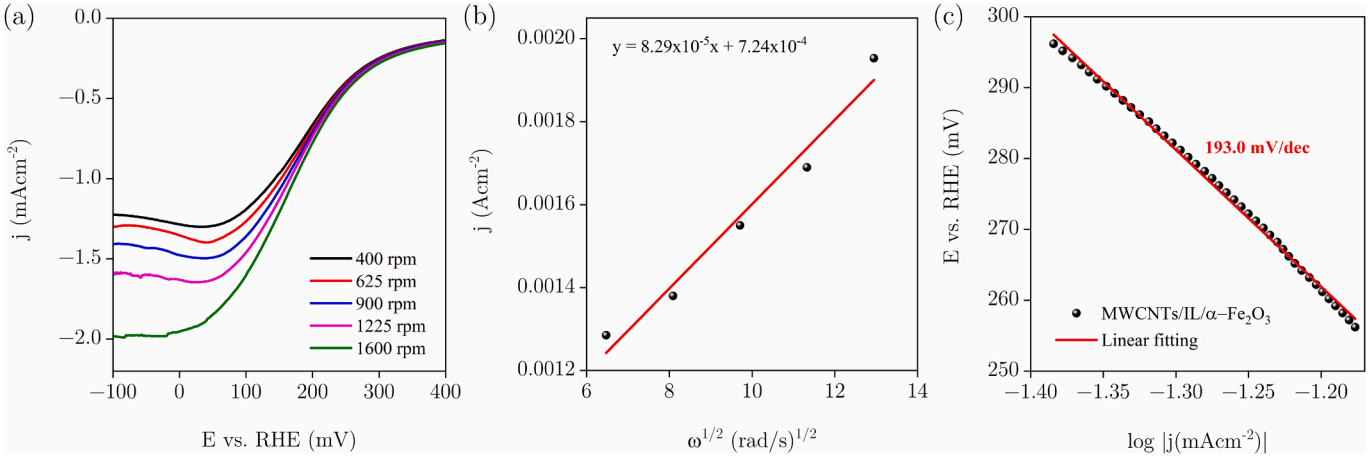


Fig. 7. Hydrodynamic study of the ORR on the MWCNTs/IL/α-Fe_2O_3 catalyst. **(a)** Polarization curves recorded at different rotation speeds in O_2-saturated 0.1 M $HClO_4$, scan rate: 50 mV/s. **(b)** Corresponding Levich plot of the limiting current density at 0 V (vs. RHE) versus the square root of the angular velocity. The red line represents the linear fit to the data. **(c)** Tafel plot derived from RDE data for the MWCNTs/IL/α-Fe_2O_3 catalyst.

0.19 V vs. RHE. To confirm that the process is predominantly diffusion-controlled, a Levich plot of limiting current density versus $\omega^{1}/^{2}$ was constructed (Fig. 7b). The plot's linearity validates the use of the Levich equation for analysis. Notably, the non-zero intercept in the plot indicates mixed kinetic-diffusion control, further supporting the notion that kinetic limitations remain. From the slope of this plot, the number of electrons transferred (n) per O_2 molecule was calculated to be 3.44. This value, while strongly indicative of a 4-electron process, is slightly lower than the n ≈ 4.0 determined from the more direct RRDE analysis. Such minor discrepancies are common and, as suggested by the Levich intercept, can be attributed to the ideal Levich model assuming a purely diffusion-limited process. At the same time, slight kinetic limitations on the catalyst surface may persist. Nonetheless, both RDE and RRDE techniques consistently demonstrate that the α-Fe_2O_3 catalyst promotes a predominantly 4-electron reduction of O_2 to H_2O.

Tafel analysis was performed by plotting potential versus the logarithm of current density (Fig. 7c). From the linear region of the plot, a Tafel slope of 193 mV/dec was calculated. This value is larger than the theoretical slopes of 60 or 120 mV/dec typically associated with a simple, single rate-determining step for ORR, indicating a more complex kinetic behavior at the catalyst. Such a high Tafel slope likely arises from a combination of both extrinsic and intrinsic factors. A primary extrinsic contributor is the uncompensated ohmic resistance within the system, which is well known to inflate measured Tafel slopes [76]. Intrinsic to the value is the inherent complexity of the ORR on the composite surface, which could involve a multistep electron-transfer mechanism or slow adsorption of reaction intermediates. Crucially, this picture of a complex mechanism influenced by both kinetic and ohmic limitations is highly consistent with the mixed kinetic-diffusion control suggested by the non-zero intercept of the Levich plot (Fig. 7b). While a precise deconvolution of these effects is beyond the scope of this study, the analysis confirms that the ORR on this composite is a mechanistically intricate process.

When evaluated alongside representative transition-metal-based ORR catalysts in acidic media (Table 2), the MWCNTs/IL/α-Fe_2O_3 electrode developed in this work exhibits a predominantly four-electron reduction pathway, with an electron-transfer number of ~4 and a low H_2O_2 yield of 10%, confirming good selectivity toward water formation. Although its E_{onset} (0.41 V) and $E_{1/2}$ (0.19 V vs RHE) are lower than those of oxide/carbon systems reported in the literature, thus indicating a relatively high overpotential for ORR in acidic medium, the present catalyst still delivers a measurable and sustained ORR response in 0.1 M $HClO_4$ over 50 cycles and 100 h of cathodic operation. These results indicate that the proposed MWCNTs/IL/α-Fe_2O_3 architecture can promote oxygen reduction under acidic conditions within the compositional platform investigated here, with favorable selectivity, stability, and a sustained electrochemical response.

Importantly, one of the main strengths of this work is the simplicity of the electrode design and preparation method. In contrast to more sophisticated literature systems that often require complex multistep syntheses, engineered active sites, or specially tailored carbon supports, the present electrode is based on a straightforward, noble-metal-free composite combining α-Fe_2O_3, MWCNTs, and $OPyPF_6$ ionic liquid. In this sense, the results demonstrate that a simple hematite-based carbonaceous architecture can induce an observable ORR response under acidic conditions while maintaining a four-electron pathway. We also further suggest that the presence of the ionic liquid may help stabilize the oxide-based interface in aggressive media and provide a useful preliminary platform for comparative studies and the further development of low-cost transition-metal oxide electrocatalysts.

Table 2
Comparison of ORR performance metrics in acidic media for selected transition metal-based catalysts supported on carbon matrices.

Catalyst	Potential window	Acidic conditions	E_{onset}	$E_{1/2}$	n (%H_2O_2)	Stability	Ref.
Fe-N@C-NH_3	1–0.2	0.1 M $HClO_4$	0.85	0.65	n.r	10 k cyc.	[77]
CeO_2/Co-N-C	1–0.3	0.5 M H_2SO_4	0.88	0.81	4.0 (25%)	10 k cyc.	[78]
CeO_2-N-C	1–0.3	0.5 M H_2SO_4	0.59	0.41	4.0 (25%)	10 k cyc.	[78]
Co-N-C	1–0.3	0.5 M H_2SO_4	0.84	0.67	4.0 (25%)	10 k cyc.	[78]
MnO/N-C	1–0.1	0.1 M $HClO_4$	0.80	0.69	3.9 (n.r)	20 k cyc.	[79]
TaO_x/CB	1–0.4	0.1 M H_2SO_4	0.94		4 (<1%)	10 k cyc.	[80]
Fe-ZrO_2/KB	1–0.1	0.1 M $HClO_4$	n.r	0.65	n.r. (<10%)	n.r	[81]
MWCNTs/IL/α-Fe_2O_3	0.5 to −0.1	0.1 M $HClO_4$	0.41	0.19	3.9 (<10%)	50 cyc. + 100 h	This work

All potentials are reported in V vs the reversible hydrogen electrode (RHE). N-C = N-doped carbon; CB = carbon black; KB = graphitized Ketjenblack carbon; MWCNTs = multi-walled carbon nanotubes; IL = ionic liquid; cyc. = cycles; n.r. = not reported.

4. Conclusions

In this work, a low-cost electrocatalyst for the oxygen reduction reaction (ORR) in acidic media was successfully designed and evaluated based on a composite of hematite ($\alpha - Fe_2O_3$), multi-walled carbon nanotubes (MWCNTs), and an N-octylpyridinium hexafluorophosphate ionic liquid (IL) binder. A systematic and preliminary comparison against other transition metal oxides, such as Co_3O_4 and $CoFe_2O_4$, conclusively demonstrated the enhanced activity of the $\alpha - Fe_2O_3$-based system. This catalyst exhibited a more positive onset potential for the ORR and a higher peak current density. This activity was further corroborated by electrochemical impedance spectroscopy measurements, which revealed that the $\alpha - Fe_2O_3$ composite exhibited the lowest charge-transfer resistance and, consequently, the fastest kinetics among the materials tested. It was determined that this enhanced activity is not merely the additive sum of its components but rather the result of a cooperative effect between the high surface area of the conductive MWCNTs/IL scaffold and the catalytically active sites of the $\alpha - Fe_2O_3$ nanoparticles. Rotating ring-disk electrode (RRDE) studies confirmed the excellent selectivity of the $\alpha - Fe_2O_3$ catalyst. It promotes the reduction of oxygen to water via a nearly complete 4-electron pathway ($n \approx 3.9–4.0$), while keeping the yield of undesirable hydrogen peroxide consistently below 10% across the relevant potential window. High-resolution XPS analysis provided critical insights into this performance, revealing that the composite undergoes a dynamic interfacial evolution during operation. The results confirmed the formation of a reduced, FeO_x layer, characterized by the partial reduction of Fe^{3+} to Fe^{2+} and a marked rise in Fe–OH/O–H species. Furthermore, the persistence of the dominant sp^2 carbon component indicated that the MWCNTs support remains chemically intact under acidic conditions. The partial conversion of the PF_6^- anion into oxyfluorophosphate and inorganic fluoride environments (Fe-F) further suggests a chemical restructuring of the interface that stabilizes the active sites.

The catalyst also demonstrated stability in acid media, with negligible degradation of its electrocatalytic performance after 50 consecutive potential cycles and 100 h of chronoamperometry. Fe leaching remained below the ICP-OES quantification limit (<0.1 mg L^{-1}), indicating negligible metal dissolution. In summary, the α-Fe_2O_3-modified MWCNTs/IL carbon paste electrode represents a simple and effective alternative to platinum-group-metal-based catalysts. Its robust activity, selectivity towards water formation, and durability in acidic conditions position it as a candidate for application in the next generation of clean energy conversion devices, such as Proton Exchange Membrane Fuel Cells (PEMFCs).

CRediT authorship contribution statement

José Ibarra: Methodology, Investigation, Formal analysis. **J.R. Sosa-Acosta:** Writing – original draft, Methodology, Investigation. **Rodrigo del Río:** Supervision, Methodology, Investigation, Conceptualization. **Rodrigo Henriquez:** Methodology, Investigation. **Ricardo Faccio:** Supervision, Methodology, Investigation, Formal analysis. **Enrique A. Dalchiele:** Writing – original draft, Methodology, Investigation. **Camila Pía Canales:** Methodology, Investigation, Formal analysis. **Roxana Arce:** Writing – review & editing, Writing – original draft, Supervision, Methodology, Investigation. **Galo Ramírez:** Writing – review & editing, Writing – original draft, Methodology, Investigation.

Declaration of competing interest

The authors declare that they have no known competing financial interests or personal relationships that could have appeared to influence the work reported in this paper.

Acknowledgments

The authors would like to acknowledge the financial support provided by: FONDECYT Projects No. 1220107 and FONDECYT Postdoctorado No. 3260523. Scholarship ANID Project No.21210433, ANID/ANILLO/ATE220024, ANID/ANILLO/ACT 240020, FONDEQUIP project: EQM 190016, Millennium Institute on Green Ammonia as Energy Vector, MIGA, ICN 2021–023, PEDECIBA, CSIC-UdelaR and ANII, all Uruguayan Institutions, CSIC (Comisión Sectorial de Investigación Científca), Universidad de la República, Montevideo, Uruguay, and PEDECIBA – Física, Uruguay, and finally DI project n° 039.317/2023, PUCV, Chile.

Appendix A. Supplementary data

Supplementary data to this article can be found online at https://doi.org/10.1016/j.apsusc.2026.168366.

Data availability

Data will be made available on request.

References

[1] G. Zuccante, M. Acciarri, C. Lo Vecchio, I. Gatto, V. Baglio, N. Pianta, R. Ruffo, L. Navarini, C. Santoro, Oxygen reduction reaction platinum group metal-free electrocatalysts derived from spent coffee grounds, Electrochim. Acta 492 (2024) 144353, https://doi.org/10.1016/j.electacta.2024.144353.
[2] J. Liu, B. Ma, Z. Chen, X. Wei, Novel strategies for low overpotential metal–air batteries, Chem. Commun. 61 (2025) 14340–14353, https://doi.org/10.1039/D5CC03685B.
[3] P. Qiu, C. Shu, Z. Gan, J. Cao, Z. Chen, H. Wu, Y. Wu, W. Tang, Low-dimensional design of precious metal-based catalysts in fuel cells, J. Power Sources 640 (2025) 236772, https://doi.org/10.1016/j.jpowsour.2025.236772.
[4] E.F. Hidayat, S.M. Juliandri, A.R.N. Zain, Advances in proton exchange membrane fuel cell (PEMFC) materials: a review of developments from 2021 to 2025, J. Power Sources 657 (2025) (2021) 238124, https://doi.org/10.1016/j.jpowsour.2025.238124.
[5] M. Piscitelli, C. Di Franco, G.V. Bianco, G. Bruno, E. Macchia, L. Torsi, G. Scamarcio, Graphene-based opto-electronic platform for ultra-sensitive biomarker detection at zeptomolar concentrations, Small Methods 9 (2025), https://doi.org/10.1002/smtd.202402026.
[6] S. Choi, C. Kim, J.M. Suh, H.W. Jang, Reduced graphene oxide-based materials for electrochemical energy conversion reactions, Carbon Energy 1 (2019) 85–108, https://doi.org/10.1002/cey2.13.
[7] J. Chen, Z. Liu, K. Feng, F. Deng, Y. Yu, Electrostatically connected Fe2O3@Ni-MOF nanosheet array heterojunction for high-performance light-assisted zinc-air batteries, Compos. B Eng. 289 (2025) 111936, https://doi.org/10.1016/j.compositesb.2024.111936.
[8] N. Xu, J. Qiao, Q. Nie, M. Wang, H. Xu, Y. Wang, X.D. Zhou, CoFe2O4 nanoparticles decorated carbon nanotubes: air-cathode bifunctional catalysts for rechargeable zinc-air batteries, Catal. Today 318 (2018) 144–149, https://doi.org/10.1016/j.cattod.2017.10.020.
[9] W. Yan, Y. Wu, Y. Chen, Q. Liu, K. Wang, N. Cao, F. Dai, X. Li, J. Jiang, Facile preparation of N-doped corncob-derived carbon nanofiber efficiently encapsulating Fe2O3 nanocrystals towards high ORR electrocatalytic activity, J. Energy Chem. 44 (2020) 121–130, https://doi.org/10.1016/j.jechem.2019.09.002.
[10] S.G. Peera, R.S. Menon, S.K. Das, A. Alfantazi, K. Karuppasamy, C. Liu, A.K. Sahu, Oxygen reduction electrochemistry at F doped carbons: a review on the effect of highly polarized C-F bonding in catalysis and stability of fuel cell catalysts, Coord. Chem. Rev. 500 (2024) 215491, https://doi.org/10.1016/j.ccr.2023.215491.
[11] Y. Liang, H. Wang, P. Diao, W. Chang, G. Hong, Y. Li, M. Gong, L. Xie, J. Zhou, J. Wang, T.Z. Regier, F. Wei, H. Dai, Oxygen reduction electrocatalyst based on strongly coupled cobalt oxide nanocrystals and carbon nanotubes, J. Am. Chem. Soc. 134 (2012) 15849–15857, https://doi.org/10.1021/ja305623m.
[12] J. Liu, M. Jiao, L. Lu, H.M. Barkholtz, Y. Li, Y. Wang, L. Jiang, Z. Wu, D. Liu, L. Zhuang, C. Ma, J. Zeng, B. Zhang, D. Su, P. Song, W. Xing, W. Xu, Y. Wang, Z. Jiang, G. Sun, High performance platinum single atom electrocatalyst for oxygen reduction reaction, Nat. Commun. 8 (2017) 15938, https://doi.org/10.1038/ncomms15938.
[13] Y. He, G. Wu, PGM-free oxygen-reduction catalyst development for proton-exchange membrane fuel cells: challenges, solutions, and promises, Acc. Mater. Res. 3 (2022) 224–236, https://doi.org/10.1021/accountsmr.1c00226.
[14] V. Men Truong, J. Richard Tolchard, J. Svendby, M. Manikandan, H.A. Miller, S. Sunde, H. Yang, D.R. Dekel, A. Oyarce Barnett, Platinum and platinum group metal-free catalysts for anion exchange membrane fuel cells, Energies (Basel) 13 (2020) 582, https://doi.org/10.3390/en13030582.

[15] J. Golubović, M. Varničić, S. Štrbac, Study of oxygen reduction reaction on polycrystalline rhodium in acidic and alkaline media, Catalysts 14 (2024) 327, https://doi.org/10.3390/catal14050327.
[16] Z. Wang, H. Yan, Z. Liu, K. Wang, M. Zhou, Z. Tong, H. Shi, F. Wang, S. Lu, Z. Ni, G. Liu, Platinum-free medium-entropy FeCoNiCu selenide/N-CNT electrocatalyst with superior ORR activity and long-term stability in alkaline medium, Int. J. Hydrogen Energy 184 (2025) 151899, https://doi.org/10.1016/j.ijhydene.2025.151899.
[17] J. Wang, Z. Huang, W. Liu, C. Chang, H. Tang, Z. Li, W. Chen, C. Jia, T. Yao, S. Wei, Y. Wu, Y. Li, Design of N-coordinated dual-metal sites: a stable and active Pt-free catalyst for acidic oxygen reduction reaction, J. Am. Chem. Soc. 139 (2017) 17281–17284, https://doi.org/10.1021/jacs.7b10385.
[18] H. Wan, M. Lv, X. Liu, G. Chen, N. Zhang, Y. Cao, H. Wang, R. Ma, G. Qiu, Activating hematite nanoplates via partial reduction for electrocatalytic oxygen reduction reaction, ACS Sust. Chem. Eng. 7 (2019) 11841–11849, https://doi.org/10.1021/acssuschemeng.9b02352.
[19] Y. Li, T. Wang, Z. Yao, Q. Chen, Q. Li, Enhancing the performance of platinum group metal-based electrocatalysts through nonmetallic element doping, Chin. J. Catal. 56 (2024) 51–73, https://doi.org/10.1016/S1872-2067(23)64569-3.
[20] A.E. Hughes, N. Haque, S.A. Northey, S. Giddey, Platinum group metals: a review of resources, production and usage with a focus on catalysts, Resources 10 (2021) 93, https://doi.org/10.3390/resources10090093.
[21] J. Zhu, A.O. Elnabawy, Z. Lyu, M. Xie, E.A. Murray, Z. Chen, W. Jin, M. Mavrikakis, Y. Xia, Facet-controlled Pt–Ir nanocrystals with substantially enhanced activity and durability towards oxygen reduction, Mater. Today 35 (2020) 69–77, https://doi.org/10.1016/j.mattod.2019.11.002.
[22] X. Tian, X.F. Lu, B.Y. Xia, X.W. (David) Lou, Advanced electrocatalysts for the oxygen reduction reaction in energy conversion technologies, Joule 4 (2020) 45–68, https://doi.org/10.1016/j.joule.2019.12.014.
[23] X. Lv, J. Gong, S. Wang, X. Yan, C. Sun, X. Hu, Z. Lai, Y. Liu, H. Wang, Z. Yuan, J. Geng, Engineering orbital hybridization in advanced electrocatalysts for energy conversion: fundamentals, modulations, and perspectives, Adv. Energy Mater. 15 (2025), https://doi.org/10.1002/aenm.202501129.
[24] Y. Chen, C. Shang, X. Xiao, W. Guo, Q. Xu, Recent progress of electrocatalysts for acidic oxygen evolution reaction, Coord. Chem. Rev. 508 (2024) 215758, https://doi.org/10.1016/j.ccr.2024.215758.
[25] X. Sun, D. Zhang, K. Xu, B. Qian, K. Chen, D. Xue, Ir cluster/Fe2O3 heterostructures on carbon nanotubes boosting oxygen evolution/reduction reactions for flexible Zn-air battery, Nano Mater. Sci. (2025), https://doi.org/10.1016/j.nanoms.2025.02.002.
[26] M.B. Stevens, M. Anand, M.E. Kreider, E.K. Price, J.Z. Zeledón, L. Wang, J. Peng, H. Li, J.M. Gregoire, J. Hummelshøj, T.F. Jaramillo, H. Jia, J.K. Nørskov, Y. Roman-Leshkov, Y. Shao-Horn, B.D. Storey, S.K. Suram, S.B. Torrisi, J. H. Montoya, New challenges in oxygen reduction catalysis: a consortium retrospective to inform future research, Energy Environ. Sci. 15 (2022) 3775–3794, https://doi.org/10.1039/d2ee01333a.
[27] L. Payattikul, C.-Y. Chen, Y.-S. Chen, M. Raja Pugalenthi, K. Punyawudho, Recent advances and synergistic effects of non-precious carbon-based nanomaterials as ORR electrocatalysts: a review, Molecules 28 (2023) 7751, https://doi.org/10.3390/molecules28237751.
[28] M. Mazzucato, L. Gavioli, V. Balzano, E. Berretti, G.A. Rizzi, D. Badocco, P. Pastore, A. Zitolo, C. Durante, Synergistic effect of Sn and Fe in Fe-Nx site formation and activity in Fe-N-C catalyst for ORR, ACS Appl. Mater. Interf. 14 (2022) 54635–54648, https://doi.org/10.1021/acsami.2c13837.
[29] X. Qu, Y. Li, G. Li, R. Ji, S. Yin, X. Cheng, C. Wang, J. Yang, Y. Jiang, S. Sun, Boosting the ORR performance of Fe-N/C catalyst via increasing the density and modifying the electronic structure of Fe-NX active sites, Electrochim. Acta 403 (2022), https://doi.org/10.1016/j.electacta.2021.139604.
[30] B. Li, R. Jervis, Advancing Fe–N–C catalysts: synthesis strategies and performance enhancements for fuel cell applications, Energy Adv. 4 (2025) 1412–1425, https://doi.org/10.1039/D5YA00256G.
[31] S. Yin, L. Chen, J. Yang, X. Cheng, H. Zeng, Y. Hong, H. Huang, X. Kuai, Y. Lin, R. Huang, Y. Jiang, S. Sun, A Fe-NC electrocatalyst boosted by trace bromide ions with high performance in proton exchange membrane fuel cells, Nat. Commun. 15 (2024), https://doi.org/10.1038/s41467-024-51858-w.
[32] H. Sun, Z. Ge, Y. Wang, D. Li, R. Peng, Z. Deng, R. Chang, W. Dong, C. Wen, J. Li, Y. Wang, S. Zhang, J. Dong, Y. Yang, H. Jin, L. Cao, Z. Zhao, Improving fuel cell performance of FeNx-based catalysts by introducing graphitic microdomains in the carbon matrix, ACS Nano 19 (2025) 23359–23369, https://doi.org/10.1021/acsnano.5c06424.
[33] W. Chen, Y. Qin, C. Heng, S. Wang, M. Ge, Y. Li, X. Wan, X. Li, J. Shui, Y. Su, D. Su, Degradation of FeNC electrocatalysts for acidic and alkaline oxygen reduction, J. Am. Chem. Soc. 147 (2025) 35730–35741, https://doi.org/10.1021/jacs.5c11985.
[34] D. Mladenović, A. Mladenović, D.M.F. Santos, A.B. Yurtcan, Š. Miljanić, S. Mentus, B. Šljukić, Transition metal oxides for bifunctional ORR/OER electrocatalysis in unitized regenerative fuel cells, J. Electroanal. Chem. 946 (2023) 117709, https://doi.org/10.1016/j.jelechem.2023.117709.
[35] H. Araújo, B. Šljukić, S. Gago, D.M.F. Santos, The current state of transition metal-based electrocatalysts (oxides, alloys, POMs, and MOFs) for oxygen reduction, oxygen evolution, and hydrogen evolution reactions, Front. Energy Res. 12 (2024), https://doi.org/10.3389/fenrg.2024.1373522.
[36] Y. Zhang, Q. Fu, B. Song, P. Xu, Regulation strategy of transition metal oxide-based electrocatalysts for enhanced oxygen evolution reaction, Acc. Mater. Res. 3 (2022) 1088–1100, https://doi.org/10.1021/accountsmr.2c00161.
[37] V. Mehta, H.S. Saini, S. Srivastava, M.K. Kashyap, K. Tankeshwar, Ultralow diffusion barrier of double transition metal MoWC monolayer as Li-ion battery anode, J. Mater. Sci. 57 (2022) 10702–10713, https://doi.org/10.1007/s10853-022-07237-1.
[38] J.X. Flores-Lasluisa, F. Huerta, D. Cazorla-Amorós, E. Morallón, Transition metal oxides with perovskite and spinel structures for electrochemical energy production applications, Environ. Res. 214 (2022) 113731, https://doi.org/10.1016/j.envres.2022.113731.
[39] M. Fatima, F. Ahmad, S. Waiza, S. Noor, A.B.M. Shafique, M.A. Ibrahim, M. I. Habib, A.S. Khan, Application of carbon-based electrocatalysts derived from waste materials in fuel cells and electrolyzers, Sust. Energy Fuels 9 (2025) 3523–3549, https://doi.org/10.1039/D5SE00303B.
[40] L. Lu, Q. Hao, W. Lei, X. Xia, P. Liu, D. Sun, X. Wang, X. Yang, Well-combined magnetically separable hybrid cobalt ferrite/nitrogen-doped graphene as efficient catalyst with superior performance for oxygen reduction reaction, Small 11 (2015) 5833–5843, https://doi.org/10.1002/smll.201502322.
[41] W. Sun, Q. Li, S. Gao, J.K. Shang, Monometallic Pd/Fe 3O 4 catalyst for denitrification of water, Appl Catal B 125 (2012) 1–9, https://doi.org/10.1016/j.apcatb.2012.05.014.
[42] C. Bathula, A. Talha Aqueel Ahmed, A. Kadam, S. Sekar, J.-H. Hwang, S.-H. Lee, H.-S. Kim, Multi-functional Co3O4 embedded carbon nanotube architecture for oxygen evolution reaction and benzoin oxidation, J. Mol. Liq. 343 (2021) 117616, https://doi.org/10.1016/j.molliq.2021.117616.
[43] Q. Wei, X. Tong, G. Zhang, J. Qiao, Q. Gong, S. Sun, Nitrogen-doped carbon nanotube and graphene materials for oxygen reduction reactions, Catalysts 5 (2015) 1574–1602, https://doi.org/10.3390/catal5031574.
[44] R. Das, B.F. Leo, F. Murphy, The toxic truth about carbon nanotubes in water purification: a perspective view, Nanoscale Res. Lett. 13 (2018) 183, https://doi.org/10.1186/s11671-018-2589-z.
[45] C. Luo, H. Sun, Z. Jiang, H. Guo, M. Gao, M. Wei, Z. Jiang, H. Zhou, S.-G. Sun, Electrocatalysts of Mn and Ru oxides loaded on MWCNTS with 3D structure and synergistic effect for rechargeable Li-O2 battery, Electrochim. Acta 282 (2018) 56–63, https://doi.org/10.1016/j.electacta.2018.06.040.
[46] K. Ichihashi, S. Muratsugu, H. Matsui, K. Higashi, O. Sekizawa, T. Uruga, M. Tada, Oxygen reduction reaction performance tuning on Pt nanoparticle/MWCNT catalysts by Gd species, J. Phys. Chem. C 124 (2020) 26925–26936, https://doi.org/10.1021/acs.jpcc.0c09308.
[47] S. Ajmal, A. Kumar, G. Yasin, M.M. Alam, M. Selvaraj, M. Tabish, M.A. Mushtaq, R. K. Gupta, W. Zhao, A microwave-assisted decoration of carbon nanotubes with Fe3O4 nanoparticles for efficient electrocatalytic oxygen reduction reaction, J. Alloys Compd. 943 (2023) 169067, https://doi.org/10.1016/j.jallcom.2023.169067.
[48] S. Singh, A. Shrivastava, D.K. Singh, M. Yadav, V. Singh, V. Rathour, A. Tiwari, I. Sinha, V. Ganesan, ZnMn2O4 spinel nanocrystals-decorated multi-walled carbon nanotubes for oxygen reduction: experimental and theoretical studies on the strong coupling facilitated four-electron selectivity, Int. J. Hydrogen Energy 56 (2024) 188–198, https://doi.org/10.1016/j.ijhydene.2023.12.157.
[49] G.R. Zhang, T. Wolker, D.J.S. Sandbeck, M. Munoz, K.J.J. Mayrhofer, S. Cherevko, B.J.M. Etzold, Tuning the electrocatalytic performance of ionic liquid modified Pt catalysts for the oxygen reduction reaction via cationic chain engineering, ACS Catal. 8 (2018) 8244–8254, https://doi.org/10.1021/acscatal.8b02018.
[50] M. George, G.R. Zhang, N. Schmitt, K. Brunnengräber, D.J.S. Sandbeck, K.J. J. Mayrhofer, S. Cherevko, B.J.M. Etzold, Effect of ionic liquid modification on the ORR performance and degradation mechanism of trimetallic PtNiMo/C catalysts, ACS Catal. 9 (2019) 8682–8692, https://doi.org/10.1021/acscatal.9b01772.
[51] J. Abraham, T. Jose, G. Moni, S.C. George, N. Kalarikkal, S. Thomas, Ionic liquid modified multiwalled carbon nanotube embedded styrene butadiene rubber membranes for the selective removal of toluene from toluene/methanol mixture via pervaporation, J. Taiwan Inst. Chem. Eng. 95 (2019) 594–601, https://doi.org/10.1016/j.jtice.2018.09.019.
[52] Y. Hu, Y. Xing, H. Yue, T. Chen, Y. Diao, W. Wei, S. Zhang, Ionic liquids revolutionizing biomedicine: recent advances and emerging opportunities, Chem. Soc. Rev. 52 (2023) 7262–7293, https://doi.org/10.1039/d3cs00510k.
[53] U. Kernchen, B. Etzold, W. Korth, A. Jess, Solid catalyst ionic liquid layer (SCILL) - a new concept to improve selectivity illustrated by hydrogenation of cyclooctadiene, Chem. Eng. Technol. 30 (2007) 985–994, https://doi.org/10.1002/ceat.200700050.
[54] S. Favero, I.E.L. Stephens, M.M. Titirici, Deconvoluting kinetics and transport effects of ionic liquid layers on FeN4-based oxygen reduction catalysts, EES Catal. 1 (2023) 742–754, https://doi.org/10.1039/d3ey00166k.
[55] A. Avid, J.L. Ochoa, Y. Huang, Y. Liu, P. Atanassov, I.V. Zenyuk, Revealing the role of ionic liquids in promoting fuel cell catalysts reactivity and durability, Nat. Commun. 13 (2022) 6349, https://doi.org/10.1038/s41467-022-33895-5.
[56] L. Gidi, R. Arce, J. Ibarra, M. Isaacs, M.J. Aguirre, G. Ramírez, Hydrogen evolution reaction highly electrocatalyzed by MWCNT/N-octylpyridinum hexafluorophosphate metal-free system, Electrochim. Acta 372 (2021) 137859, https://doi.org/10.1016/j.electacta.2021.137859.
[57] F. Fuenzalida, D. Aravena, C. García, M. García, R. Arce, G. Ramírez, C. Díaz, M. Isaacs, M. del C. Arévalo, M.J. Aguirre, Effect of the substituent of the cation of N-octylpyridinium hexafluorophosphate in the electrical and electrochemical response of carbon paste electrodes modified with these ionic liquids, Electrochim. Acta 258 (2017) 959–969, https://doi.org/10.1016/j.electacta.2017.11.147.
[58] S. Díaz-Coello, D. Winkler, C. Griesser, T. Moser, J. Rodríguez, J. Kunze-Liebhäuser, G. García, E. Pastor, Highly active W2C-based composites for the HER in alkaline solution: the role of surface oxide species, ACS Appl. Mater. Interf. 16 (2024) 21877–21884, https://doi.org/10.1021/acsami.4c01612.

[59] S. Díaz-Coello, M.M. Afonso, J.A. Palenzuela, E. Pastor, G. García, Composite materials from transition metal carbides and ionic liquids as electrocatalyst for hydrogen evolution in alkaline media, J. Electroanal. Chem. 898 (2021) 115620, https://doi.org/10.1016/j.jelechem.2021.115620.
[60] J. Ibarra, M.J. Aguirre, R. del Río, R. Henriquez, R. Faccio, E.A. Dalchiele, R. Arce, G. Ramírez, α-Fe2O3/, Co3O4/, and CoFe2O4/MWCNTs/ionic liquid nanocomposites as high-performance electrocatalysts for the electrocatalytic hydrogen evolution reaction in a neutral medium, Int. J. Mol. Sci. 25 (2024) 7043, https://doi.org/10.3390/ijms25137043.
[61] S. Tajik, H. Beitollahi, F.G. Nejad, M. Safaei, K. Zhang, Q. Van Le, R.S. Varma, H. W. Jang, M. Shokouhimehr, Developments and applications of nanomaterial-based carbon paste electrodes, RSC Adv. 10 (2020) 21561–21581, https://doi.org/10.1039/D0RA03672B.
[62] I.C.B. Alves, J.R.N. Santos, D.S.S. Viégas, E.P. Marques, C.A. Lacerda, L. Zhang, J. Zhang, A.L.B. Marques, Nanoparticles of Fe2O3 and Co3O4 as efficient electrocatalysts for oxygen reduction reaction in acid medium, J. Braz. Chem. Soc. 30 (2019) 2681–2690, https://doi.org/10.21577/0103-5053.20190195.
[63] E.R. Vago, E.J. Calvo, Electrocatalysis of oxygen reduction at Fe,O, oxide electrodes in alkaline solutions *, Elsevier Seq. S.A. (1992).
[64] M.A. Henderson, Low temperature oxidation of Fe2+ surface sites on the (2 × 1) reconstructed surface of α-Fe2O3(011-2), Surf. Sci. 604 (2010) 1197–1201, https://doi.org/10.1016/j.susc.2010.04.002.
[65] C. Goswami, K.K. Hazarika, P. Bharali, Transition metal oxide nanocatalysts for oxygen reduction reaction, Mater. Sci. Energy Technol. 1 (2018) 117–128, https://doi.org/10.1016/j.mset.2018.06.005.
[66] V. Vivier, M.E. Orazem, Impedance analysis of electrochemical systems, Chem. Rev. 122 (2022) 11131–11168, https://doi.org/10.1021/acs.chemrev.1c00876.
[67] S. Das, A. Banerjee, U. Nandi, A. Ghosh, Critical review on the analysis of electrochemical impedance spectroscopy data, J. Appl. Phys. 138 (2025), https://doi.org/10.1063/5.0275205.
[68] S. Dong, Y. Lyu, Z.-S. Guo, Effect of carbon nanotubes conductors on electrolyte wettability and electrochemical performance of lithium-ion battery electrodes, ChemSusChem 18 (2025) e202402517, https://doi.org/10.1002/cssc.202402517.
[69] E.B. Boz, M. van der Heijden, R.R. Jacquemond, P. Boillat, J. Hjelm, A. Forner-Cuenca, Correlating electrolyte infiltration with accessible surface area in macroporous electrodes using neutron radiography, J. Electrochem. Soc. 171 (2024) 053509, https://doi.org/10.1149/1945-7111/ad4ac7.
[70] S.S. Li, W.J. Li, T.J. Jiang, Z.G. Liu, X. Chen, H.P. Cong, J.H. Liu, Y.Y. Huang, L. N. Li, X.J. Huang, Iron oxide with different crystal phases (α- and γ-Fe2O3) in electroanalysis and ultrasensitive and selective detection of lead(II): an advancing approach using XPS and EXAFS, Anal. Chem. 88 (2016) 906–914, https://doi.org/10.1021/acs.analchem.5b03570.
[71] P.S. Bagus, C.J. Nelin, C.R. Brundle, B.V. Crist, N. Lahiri, K.M. Rosso, Origin of the complex main and satellite features in Fe 2p XPS of Fe2O3, PCCP 24 (2022) 4562–4575, https://doi.org/10.1039/d1cp04886d.
[72] A.P. Grosvenor, B.A. Kobe, M.C. Biesinger, N.S. McIntyre, Investigation of multiplet splitting of Fe 2p XPS spectra and bonding in iron compounds, Surf. Interf. Anal. 36 (2004) 1564–1574, https://doi.org/10.1002/sia.1984.
[73] M.C. Biesinger, B.P. Payne, A.P. Grosvenor, L.W.M. Lau, A.R. Gerson, R.S.C. Smart, Resolving surface chemical states in XPS analysis of first row transition metals, oxides and hydroxides: Cr, Mn, Fe, Co and Ni, Appl. Surf. Sci. 257 (2011) 2717–2730, https://doi.org/10.1016/j.apsusc.2010.10.051.
[74] P. Marcel, Atlas D'equilibres Electrochimiques, Gauthier-Villars, 1963. https://books.google.cl/books?id=bGLFzwEACAAJ.
[75] M. Kapkowski, S. Kotowicz, K. Kocot, M. Korzec, J. Kubacki, M. Zubko, K. Aniołek, U. Siudyga, T. Siudyga, J. Polanski, From recycled polyethylene terephthalate waste to high-value chemicals and materials: a zero-waste technology approach, Energies (Basel) 18 (2025) 4375, https://doi.org/10.3390/en18164375.
[76] D. Van Der Vliet, D.S. Strmcnik, C. Wang, V.R. Stamenkovic, N.M. Markovic, M.T. M. Koper, On the importance of correcting for the uncompensated Ohmic resistance in model experiments of the oxygen reduction reaction, J. Electroanal. Chem. 647 (2010) 29–34, https://doi.org/10.1016/j.jelechem.2010.05.016.
[77] A. Madrid, Á. Tolosana-Moranchel, Á. García, S. Rojas, F. Bartolome, E. Pakrieva, L. Simonelli, G. Martinez, J.L. Hueso, J. Santamaria, Laser driven generation of single atom Fe-N-C catalysts for the oxygen reduction reaction, Chem. Eng. J. 498 (2024), https://doi.org/10.1016/j.cej.2024.155363.
[78] S. Wang, Y. Guo, Z. Zhang, Y. Zheng, Z. Zhuang, W. Yan, J. Zhang, Rare earth metal oxides tailored Co-N-C catalysts for enhanced acidic oxygen reduction reaction activity and stability, Chem. Eng. J. 535 (2026) 175267, https://doi.org/10.1016/j.cej.2026.175267.
[79] W. Hao, S.H. Lee, S.G. Peera, Xerogel-derived manganese Oxide/N-doped carbon as a non-precious metal-based oxygen reduction reaction catalyst in microbial fuel cells for energy conversion applications, Nanomaterials 13 (2023), https://doi.org/10.3390/nano13222949.
[80] J. Seo, D.H. Anjum, K. Takanabe, J. Kubota, K. Domen, Electrodeposited ultrafine TaOx/CB catalysts for PEFC cathode application: their oxygen reduction reaction kinetics, Electrochim. Acta 149 (2014) 76–85, https://doi.org/10.1016/j.electacta.2014.10.073.
[81] P. Madkikar, D. Menga, G.S. Harzer, T. Mittermeier, A. Siebel, F.E. Wagner, M. Merz, S. Schuppler, P. Nagel, A.B. Muñoz-García, M. Pavone, H.A. Gasteiger, M. Piana, Nanometric Fe-substituted ZrO 2 on carbon black as PGM-free ORR catalyst for PEMFCs, J. Electrochem. Soc. 166 (2019) F3032–F3043, https://doi.org/10.1149/2.0041907jes.